Impact of pyrolysis heating methods on biochars with enhanced CO2/N2 separation and their incorporation in 3D-printed composites

Original
Impact of pyrolysis heating methods on biochars with enhanced CO2/N2 separation and their incorporation in 3D-printed composites / Correia, Inês; Ilkaeva, Marina; Castellino, Micaela; Bocchini, Sergio; Novais, Rui M.; Mafra, Luís; Gonçalves, Nuno P. F.; Lourenço, Mirtha A. O.. - In: JOURNAL OF ENVIRONMENTAL CHEMICAL ENGINEERING. - ISSN 2213-3437. - ELETTRONICO. - 12:5(2024), pp. 1-13. [10.1016/j.jece.2024.113875]

Publisher:
Elsevier

Published
DOI:10.1016/j.jece.2024.113875

Journal of Environmental Chemical Engineering 12 (2024) 113875

Contents lists available at ScienceDirect

Journal of Environmental Chemical Engineering

journal homepage: www.elsevier.com/locate/jece

Impact of pyrolysis heating methods on biochars with enhanced CO_2/N_2 separation and their incorporation in 3D-printed composites

Inês Correia [a], Marina Ilkaeva [a,b], Micaela Castellino [c,d], Sergio Bocchini [c,d], Rui M. Novais [e], Luís Mafra [a], Nuno P.F. Gonçalves [a,*], Mirtha A.O. Lourenço [a,*]

[a] CICECO - Instituto de Materiais de Aveiro, Department of Chemistry, University of Aveiro, Campus Universitário de Santiago, Aveiro 3810-193, Portugal
[b] Department of Chemical and Environmental Engineering, University of Oviedo, Av. Julián Clavería 8, Oviedo 33006, Spain
[c] Department of Applied Science and Technology (DISAT), Politecnico di Torino, Corso Duca degli Abruzzi 24, Torino 10129, Italy
[d] Center for Sustainable Future Technologies (CSFT), Istituto Italiano di Tecnologia (IIT), Via Livorno, 60, Torino 10144, Italy
[e] Dept. of Materials and Ceramic Engineering/CICECO-Aveiro Institute of Materials, University of Aveiro, Campus Universitário de Santiago, Aveiro 3810-193, Portugal

ARTICLE INFO

Keywords:
Pyrolysis
Biochar
Additive manufacturing
Adsorption
CO_2 separation

ABSTRACT

N-doped biochars, derived from chitosan sourced from waste crustaceous shells, were produced via microwave-assisted pyrolysis at temperatures ranging from 400 to 800 °C to enhance CO_2 and N_2 separation. Their performance was compared with biochars from conventional pyrolysis. Microwave-derived biochars exhibited superior CO_2 adsorption capacity at 25 °C and 100 kPa (0.78 – 1.56 mmol g^{-1}) compared to conventionally produced ones (0.55 – 1.43 mmol g^{-1}). Increasing the pyrolysis temperature up to 600 °C significantly improved biochar properties, including surface area, pore volume, and CO_2 adsorption capacity. Microwave-derived biochar featured enhanced surface area, larger pore volumes, and unique morphologies, requiring, on average, 61 % less preparation time. The higher ultramicroporosity and N-species concentration correlated with superior performance in the biochar produced at 600 °C. In gas mixture experiments (20 % CO_2 and 80 % N_2) under flow conditions, these biochars showed rapid adsorption/desorption rates due to enhanced macroporosity at samples produced at 600 and 800 °C, facilitating gas diffusion along the ultramicropores. Adsorption heat analysis indicated that the CO_2 adsorption is predominantly driven by physisorption, supported by complete sample regeneration when applying N_2 flux or increasing the temperature during desorption. The study also explores the feasibility of 3D-printing a composite using the most effective biochar and inorganic polymers sourced from waste, presenting potential benefits for industrial applications.

1. Introduction

Human activities, particularly the increased use of fossil fuels, generate substantial amounts of CO_2, the primary greenhouse gas responsible for global warming. There is a pressing need to curb these emissions, necessitating the development of effective CO_2 capture systems. While chemical absorption, particularly amine scrubbing, has been a conventional technology, it faces significant challenges, such as equipment corrosion, high solvent regeneration costs, and sorbent loss due to amine degradation [1–7]. In this context, solid sorbents emerge as a more attractive technology for large-scale post-combustion CO_2 capture application if efficient, regenerable, and obtained from sustainable sources [1]. Among these, carbon-based materials stand-out as physisorbents with a high potential for CO_2 capture [8]. Compared to other adsorption processes, they are less susceptible to moisture, have high adsorption capacity at ambient pressure, are more thermally stable, are easily regenerable, and require less energy [9–11]. Despite these advantages, many carbon-based CO_2 adsorbents face limitations in selectivity for CO_2/N_2 separation processes or present cost challenges [12].

Biochar, a product of biomass pyrolysis, possesses distinctive characteristics, namely high thermal and chemical stability, diverse chemical compositions, and customizable surface features (that can be attained depending on the biomass source and synthesis conditions) [13, 14]. Beyond its technical merits, using biomass for biochar synthesis supports sustainable waste management practices, contributing to reduced carbon emissions and fostering a circular economy [15]. Compared to activated carbon, a benchmark competitor in adsorption applications, biochar is a more sustainable and cost-effective option [7,

---

* Corresponding authors.
E-mail addresses: nunopfgoncalves@ua.pt (N.P.F. Gonçalves), mirtha@ua.pt (M.A.O. Lourenço).

https://doi.org/10.1016/j.jece.2024.113875
Received 11 April 2024; Received in revised form 15 August 2024; Accepted 16 August 2024

16–18], it offers simpler regeneration, operational efficiency at lower temperatures, and a synthesis procedure that does not require activation [15,19–25].

Our group devised a strategy to produce self-standing N-doped biochars from chitosan, a chitin derivative found in crustacean shells. This approach aimed to create selective sorbents for efficiently capturing CO_2 from mixtures containing CH_4 and/or N_2 while ensuring ease of handling in industrial settings [5,12]. To achieve this, N-doped biochar sorbents were produced by first dissolving chitosan. Then, the study examined the effects of different drying techniques (exposure to air at room temperature for 30 days, 40 °C oven for 24 h, supercritical CO_2, and freeze-drying) and pyrolysis temperatures (400, 600, and 800 °C) using conventional assisted heating. The investigation revealed significant impacts on the textural characteristics of biochar materials. The findings indicated that variations in the synthesis conditions primarily influenced the quantity and types of N-species, along with microporosity. These factors were found to be correlated with the CO_2 adsorption separation behavior of the biochar materials. For instance, X-ray Photoelectron Spectroscopy (XPS) analysis unveiled the transformation of amino groups from chitosan into pyridinic-N, pyrrolic-N, graphitic center-N, graphitic valley-N or pyridine-N oxide species during pyrolysis [5,12]. Elevating the pyrolysis temperature increased the abundance of the latter two N-type species and the ultramicroporosity [12], which are advantageous for CO_2 uptake. While the freeze-dried material pyrolyzed at 600 °C exhibited optimal CO_2 adsorption capacity (1.6 mmol g^{-1} at 100 kPa and 25 °C), the synthesis complexity raised concerns about cost and time [12]. Recently, a solvent-free method, using chitosan as a precursor and $NaNH_2$ as an activator, produced powder N-doped porous carbon showcasing efficient and reversible CO_2 adsorption performance (1.70 – 6.33 mmol g^{-1} at 25 °C and 100 kPa) [19].

To address concerns related to the costs of pyrolysis equipment and energy consumption, we turn our attention to microwave (MW) pyrolysis as a cost-effective, efficient, and rapid alternative to conventional furnaces [20–24]. Notably, MW pyrolysis not only offers economic advantages but also excels in energy recovery and boasts lower carbon emissions [15,25,26]. A study in which rice straw was used to produce biochar for CO_2 capture using microwave pyrolysis allowed for biochar production with lower time, cost, and energy consumption while also achieving 14 % higher values of CO_2 adsorption capacity [27]. Another study's findings, using sewage sludge and leucaena wood through microwave pyrolysis concluded that this technique was feasible since it produced biochar with high CO_2 adsorption capacity (0.22 – 1.41 mmol g^{-1}) [28].

This study delves into a comprehensive investigation of the impact of different heating methods (conventional- and MW-assisted heating) and pyrolysis temperatures (400, 600, and 800 °C) on the textural properties and CO_2 adsorption behavior of N-doped biochars. Combining advanced characterization techniques such as XPS, electron microscopy, and gas sorption isotherms, our objective is to attain a comprehensive molecular-level understanding of biochar synthesis and CO_2 adsorption mechanisms. Our research specifically evaluates the microstructure effects on CO_2 adsorption capacity, kinetics, heat of adsorption, and selectivity for CO_2/N_2 separation through both applying the Ideal Adsorption Solution Theory (IAST) to the pure gas adsorption isotherms and isothermal adsorption-desorption experiments under flow conditions of a mixture of CO_2 (20 % vol) and N_2 (80 % vol) over the time. Additionally, we explore the feasibility of incorporating biochar into 3D-printed inorganic polymers (IPs) from waste sources to produce CO_2 adsorbents with open-porosity. This approach may help prevent the pressure drop issues commonly linked with powder adsorbents and enable the use of residues, thereby enhancing the sustainability of the adsorbents. The knowledge acquired from this study can catalyze the development of more efficient and sustainable CO_2 biochar/IPs adsorbents, with tunable geometries, thereby contributing to enhanced CO_2 capture solutions.

2. Materials and methods

2.1. Materials

Chitosan powder with a medium molecular weight, a degree of deacetylation of 75 – 85 %, and a low viscosity (200 – 800 cps for 1 % acetic acid) from Sigma Aldrich was used to prepare biochar. For the ink preparation, red mud (RM, supplied by a bauxite mining company, Table S1 [29]) was dried, ground, and sieved to $<$ 75 µm, while metakaolin (MK, ArgicalTM M1200S; Univar®, Table S1 [29]), sodium silicate (Chem-Lab, Belgium), sodium hydroxide (ACS reagent, 97 %, Sigma Aldrich), and polyethylene glycol (PEG-600, Alfa Aesar) were employed without prior treatment.

2.2. Pyrolysis

N-doped biochars were obtained by pyrolyzing commercial chitosan at different temperatures (400, 600, and 800 °C) using conventional- and microwave-assisted heating methods. For the conventional heating method, the chitosan powder was placed in a quartz sample holder in a vertical TMAX-VTL1200 furnace under N_2 flow. The pyrolysis process was carried out using a two-step heating procedure, as previously described by Lourenço *et al.* [30]: (i) 5 °C min^{-1}, 200 °C, 2 h and (ii) 5 °C min^{-1}, final temperature, 2 h. The resulting biochars were denoted as CTOP*x*, where *x* corresponds to the final temperature (400, 600 and 800 °C). For the microwave-assisted method, the Phoenix™ Microwave Muffle Furnace was used under N_2 flow and heating procedures set for each pyrolysis temperature: (i) 5 °C min^{-1}, 200 °C, 5 min and (ii) 5 °C min^{-1}, final temperature, 20 min. The resulting biochars were named as CTOP*x*MW, where *x* corresponds to the final temperature (400, 600, and 800 °C). Table S2 shows the total pyrolysis time for the microwave heating and conventional heating pyrolysis time and the determined yield for each biochar. Results revealed a decrease in biochar yield as the pyrolysis temperature increased and the yields obtained for both heating methods were similar regardless of the temperature.

2.3. Additive manufacturing

2.3.1. Ink optimization

The ink for direct ink writing (DIW) was prepared by incorporating biochar in the previously described red mud/metakaolin-based composition [29]. In detail, the solid raw materials were mixed with the alkaline activator solution, previously obtained by mixing 100 g of sodium silicate with a ratio of $SiO_2/Na_2O = 3.09$, 14.16 g of sodium hydroxide, and 13.39 g of water. Polyethylene glycol was also added to adjust the rheological properties. To evaluate the effect of biochar in the 3D-printed IPs, an ink without biochar (labeled as 3D-RM/MK) was initially optimized by blending 50 wt% of RM with 50 wt% of MK and the activator solution in a solid/liquid ratio to obtain desired properties for suitable DIW extrusion. The best-performing biochar (B) (sample CTOP600MW) was blended with the previous RM/MK-based ink in a 20 wt% amount selected as a proof-of-principle, denoted as 3D-B/RM/MK. Finally, the above-described compositions were mixed in a planetary centrifugal mixer (ARE–250) at 800 rpm for 6 min before being carefully inserted in the designated syringes.

2.3.2. Direct ink writing (DIW)

3D-printed structures were prepared by DIW using a 3D Inks, LLC, USA (Model EBRD-A32). A computer-aided direct-write software (RoboCAD 3.0, 3-D Inks, USA) was used to control the 3-axis motion and print a scaffold pattern previously designed using CAD software (FreeCAD, version 0.18). The optimized ink was loaded into a 3 mL syringe (Nordson, USA) and extruded at room temperature through a conical nozzle with a diameter of 410 µm (Nordson, USA) at an extrusion speed of 10 mm/s onto an aluminum oxide support. 3D scaffolds with 5 × 5 mm base and 6 mm height were obtained, composed of 20 layers with

6 parallel filaments rotated 90° in the subsequent layer and assembled. The interconnectivity between pores was defined by specifying a 300 μm distance between filaments. After extrusion, samples were kept in controlled humidity (80 %) at room temperature for 24 h. Later, the samples were cured at 40 °C for 48 h to speed up the polymerization reactions. After 14 days of curing, the structures were used.

2.4. Characterization

The textural properties of the biochar samples, as well as the 3D-printed carbon/IPs composites, were evaluated by Elemental Analysis (EA), X-ray Photoelectron Spectroscopy (XPS), Fourier Transform Infrared Spectroscopy (FTIR), X-ray Diffraction Analysis (XRD), Scanning Electron Microscopy (SEM), Energy-Dispersive X-ray Spectroscopy (EDS), Optical Microscopy, Thermogravimetric Analysis (TGA) and CO_2 and N_2 adsorption-desorption isotherms. The equipment and experimental parameters used are described in the Supplementary Material (SM).

2.4.1. CO_2 and N_2 adsorption and selectivity

Pure CO_2 and N_2 gas adsorption isotherms were measured on the biochar and 3D-printed sorbents using a volumetric apparatus (BELSORP MAX II). Prior to analysis, the samples were degassed under vacuum at 120 °C with a heating rate of 5 °C min^{-1} for 6 h. The gas exposure sequence included N_2 at −196 and 25 °C, followed by CO_2 at 0 and 25 °C.

CO_2 and N_2 pure component adsorption isotherm at 25 °C were fitted using the Virial and Freundlich-Langmuir models, and the second and third Virial coefficients were employed to account for the non-ideality of the gas phase. After fitting the CO_2 and N_2 adsorption isotherms at 25 °C using the Virial fitting, the Henry's constants (K_H) and Virial coefficients (C_1, C_2, and C_3) were obtained. Additionally, the ratio of the K_H derived from pure CO_2 and N_2 adsorption isotherms at 25 °C was determined to provide information for the selectivity and assess the affinity of CO_2 for the adsorbent surface.

Furthermore, according to Myers *et al.* [31], the Ideal Adsorption Solution Theory (IAST) was applied to the single-component adsorption isotherms of CO_2 and N_2 at 25 °C, from 0 to 90 kPa after the fitting via the Freundlich-Langmuir approach described by Nuhnen and Janiak [32] in the Origin software (OriginLab). 20 % CO_2 and 80 % N_2 were chosen as the molar fractions of the gas phase for a more accurate comparison with most literature studies.

2.4.2. CO_2/N_2 adsorption-desorption isotherms under continuous flux

The evaluation of CO_2 adsorption efficiency in the presence of N_2 gas was carried out using a Thermogravimetric Analyzer (TGA, NETZSCH TG 209F1 Libra) at a constant temperature of 35 °C and an ambient pressure of approximately 100 kPa. Approximately 10 mg of the material underwent a thorough degassing process. The samples were subjected to a temperature increase up to 120 °C at a heating rate of 40 °C min^{-1}, all while under vacuum conditions (1.0 $\times 10^{-2}$ mbar) for 360 min. Upon completion of the heating phase, the samples were cooled back to 35 °C at a reduced rate of 2 °C min^{-1}.

Following the thermal treatment, the biochar sorbents were exposed to a continuous flow of pure N_2 gas (40 mL min^{-1}) at standard atmospheric pressure for 60 min to ensure weight stabilization. This step was succeeded by the introduction of a CO_2/N_2 gas mixture (comprising 20 vol% CO_2, with a total flow rate maintained at 40 mL min^{-1}) over the samples for 120 minutes, keeping both CO_2 and N_2 flow rates steady throughout the process. The net weight change observed before and after CO_2 adsorption served as a measure of the quantity of CO_2 adsorbed by the materials.

Finally, the CO_2 desorption behavior was investigated by switching back to a pure N_2 gas atmosphere (flow rate = 40 mL min^{-1}) under ambient pressure conditions for 60 minutes where the released value was assessed. Then, the temperature was gradually increased to 120 °C at a heating rate of 40 °C min^{-1}, thereby assessing the complete reversibility of the CO_2 desorption process for practically all the samples.

2.4.3. Isosteric enthalpy of adsorption (ΔH_{ads})

The ΔH_{ads} was determined from the CO_2 adsorption isotherms obtained at two different temperatures (0 and 25 °C) which were fitted via the Freundlich-Langmuir model in the Origin software (OriginLab). Subsequently, the ΔH_{ads} values were calculated employing the Clausius-Clapeyron approach as outlined by Nuhnen and Janiak [32].

3. Results and discussion

3.1. CO_2 and N_2 adsorption in biochar sorbents

Pure CO_2 and N_2 adsorption isotherms at 25 °C (Fig. 1(a)) were registered to obtain the adsorption capacity and selectivity for all the biochar sorbents. Table 1 displays the determined Virial coefficients (C_1, C_2, and C_3) and Henry constants (K_H) for the adsorption data by applying the Virial model. The adsorption isotherms illustrate that independently of the pyrolysis heating procedure, all biochar sorbents seem to preferentially adsorb CO_2 than N_2, which is visible by the non-existent adsorption capacity for N_2 at 25 °C. Thus, it is possible to generalize that these materials have good potential for separating CO_2 from N_2. Focusing on the CO_2 isotherms, all pyrolyzed chitosan-derived biochars present the same CO_2 adsorption trend with the materials produced at 600 °C obtaining the highest values of adsorption capacity (n_{ads}(CTOP600) = 1.43 mmol g^{-1} and n_{ads}(CTOP600MW) = 1.56 mmol g^{-1}). An increase in temperature from 600 to 800 °C resulted in a slight decrease in adsorption capacity, while the value obtained for the sample pyrolyzed at 600 °C was almost 3-fold the one obtained at 400 °C. Additionally, the biochars obtained employing the MW-assisted heating method have higher CO_2 adsorption capacity than the ones from the conventional heating showing that not only is the pyrolysis process reduced in time but also the CO_2 adsorption capacity is slightly enhanced.

For the practical application of biochar, the assessment of the selectivity of CO_2 over N_2 is essential. Table 1 presents the results of the determination of the Henry constants (K_H) and Virial coefficients (C_1, C_2, and C_3) for each material and adsorbed gas. When closely comparing the K_H of each biochar sample for CO_2 it can be concluded that the samples with higher affinity to CO_2 are CTOP600 (K_H = 182 $\times 10^{-3}$ mmol^{-1} kPa^{-1}) and CTOP600MW (K_H = 316 $\times 10^{-3}$ mmol^{-1} kPa^{-1}) due to their higher K_H values. Concerning N_2 adsorption, CTOP600MW and CTOP800MW exhibited the highest K_H values (2.01 $\times 10^{-3}$ and 2.75 $\times 10^{-3}$ mmol^{-1} kPa^{-1}, respectively). These results indicate an increased affinity for N_2 as the temperature rises during MW-assisted pyrolysis. In the selectivity study, it is interesting to note that CTOP800 had the highest selectivity rate (352), even though it did not have the highest K_H value for CO_2. This is because its K_H value for N_2 was one of the lowest among the materials.

The selectivity was also studied through the Myers *et al.* [31] method using the ideal adsorption solution theory (IAST) applied to the single-component adsorption isotherms of CO_2 and N_2 at 25 °C, from 0 to 100 kPa after the fitting via the Freundlich-Langmuir approach described by Nuhnen and Janiak [32]. All the determined constants regarding the Freundlich-Langmuir fitting are summarized in Table S3. The selectivity results are illustrated in Fig. 1(b) which shows that CTOP600 and CTOP600MW have the highest selectivity values (134 and 46.5 at 100 kPa, respectively) followed by the material CTOP800MW (22). These results indicate that these samples are the most selective to CO_2 as suggested previously by the CO_2/N_2 adsorption isotherms at 25 °C (Fig. 1) and the derived Henry constants, which assess the material affinity towards CO_2 (Table 1). All samples exhibit higher selectivity to CO_2 at low pressures (0 – 20 kPa). This behavior seems to be common among other studies in the literature [33,34].

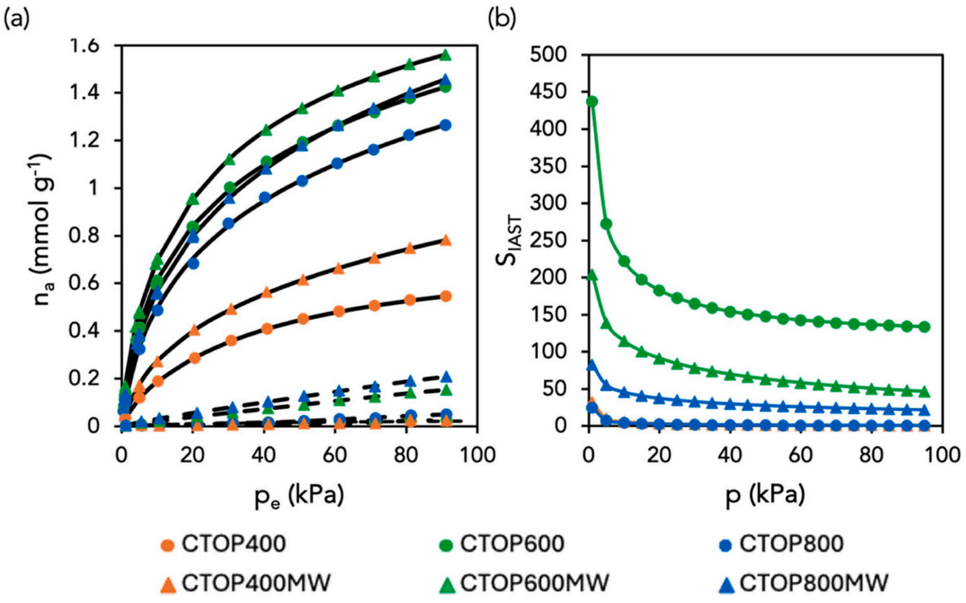

Fig. 1. (a) Adsorption isotherms of pure CO_2 (solid lines) and N_2 (dashed lines) gases at 25 °C of the biochar samples pyrolyzed in the conventional furnace (circles) and microwave furnace (triangles), at 400 (orange color), 600 (green color) and 800 °C (blue color). The solid and dashed lines represent the fits of the Virial isotherm model to the experimental data; (b) Comparative selectivity rate at 25 °C for all the biochar samples except for CTOP400 (negligible amounts of N_2 adsorption capacity). The gas phase was selected to consist of 20 % CO_2 and 80 % N_2 in terms of molar fractions.

Table 1
Henry constants and Virial coefficients of the biochar materials calculated from CO_2 and N_2 at 25 °C.

Gas	Sample	K_H x 10^{-3} (mmol^{-1} g^{-1} kPa^{-1})	C_1 (g mol^{-1})	C_2 (g mol^{-1})^2	C_3 (g mol^{-1})^3	K^{CO2}/ K^{N2}
CO_2	CTOP400	41.4	3.50	0	0	-
	CTOP400MW	45.8	2.15	0	0	279
	CTOP600	182	1.72	0	0	334
	CTOP600MW	316	3.09	−1.73	0.61	157
	CTOP800	113	1.65	0	0	352
	CTOP800MW	143	1.70	−0.13	0	52
N_2	CTOP400	-	-	-	-	
	CTOP400MW	0.16	−22.00	0	0	
	CTOP600	0.54	21.10	0	0	
	CTOP600MW	2.01	1.22	0	0	
	CTOP800	0.32	−10.60	0	0	
	CTOP800MW	2.75	0.90	0	0	

Fig. 2(a) displays the CO_2 adsorption isotherms over time under a continuous gas flux consisting of 80 vol% N_2 and 20 vol% CO_2 at 35 °C and atmospheric pressure for all biochar sorbents and Fig. 2(b) summarizes the weight changes of the adsorption/desorption analysis for these biochar sorbents. The observed weight increase across all samples upon introducing CO_2 gas indicates the selectivity of biochar sorbents for CO_2 over N_2. Furthermore, the highest values of CO_2 adsorption capacity over N_2 correspond to the samples CTOP600MW (0.894 mmol g^{-1}) and CTOP800MW (0.807 mmol g^{-1}). Following the adsorption capacity parameters in Fig. 2(b) while increasing the pyrolysis temperature, it can be concluded that when increasing the temperature from 400 to 600 °C the adsorption capacity is almost tripled for both heating methods (CTOP400 – 0.274 mmol g^{-1}; CTOP400MW – 0.365 mmol g^{-1}). On the other hand, the samples pyrolyzed at 800 °C show a slight decrease in adsorption capacity (CTOP800 – 0.489 mmol g^{-1}; CTOP800MW – 0.807 mmol g^{-1}). This behavior is consistent with the findings from Fig. 1. All samples, apart from CTOP800, exhibit a similar pattern, attaining 76 – 88 % of the total CO_2 adsorption within the initial 10 min (Fig. 2(a)). This indicates that most of the studied biochar sorbents have fast adsorption kinetics. In contrast, CTOP800 presents a slower adsorption behavior, reaching only 44 % of the total CO_2 adsorption in the same 10 min timeframe. This suggests that CTOP800 requires a longer duration to reach the maximum CO_2 adsorption capacity. The CTOP800MW has slightly higher adsorption kinetics than CTOP600MW, however, this material achieves a higher CO_2 adsorption capacity overall.

The desorption efficiency of the materials was also studied. Most materials depicted high desorption efficiencies releasing between 45 – 67 % of the CO_2 captured in less than 10 minutes frame (Fig. 2(a)) with the highest values being attributed to samples CTOP800MW (67 %), CTOP600 (60 %) and CTOP600MW (55 %). In contrast, CTOP800 only desorbed 24 % of its adsorbed CO_2 at the same adsorption time. Independently of the sample, most CO_2 captured was desorbed by only switching the gas mixture to pure N_2 flow.

Complete regeneration of the samples can be achieved by raising 120 °C, which induces further CO_2 desorption (Fig. 2). These conclusions, based on the materials adsorption and desorption properties, immediately relate to their possible use in cyclic adsorption-desorption measurements under industrial operating conditions.

3.2. Comparison with reported biochar adsorbents

Table 2 presents reported biochar sorbents by other studies in which the capacities for CO_2 and N_2 adsorption and CO_2/N_2 separation are compared with the two best-performing sorbents from this study (CTOP600 and CTOP600MW).

All the biochar material displayed did not undergo any chemical or physical modification as well as the materials prepared in this study, so they are to be considered pristine biochars and not engineered/modified biochars. The temperature used for comparison was 600 °C to directly compare with the previously stated as the two best-performing sorbents from this study. A diversity of feedstocks can be found in the literature as precursors for biochar preparation. In the first study, sugarcane bagasse and hickory wood were both oven-dried and converted into biochar through slow pyrolysis in a furnace in a N_2 environment at 600 °C. The biochars presented a CO_2 uptake at 25 °C of 1.36 and 1.18 mmol g^{-1}, respectively [7]. In one of our group's studies, sponge-like biochar sorbents were prepared from the dissolution of chitosan followed by freeze-drying methodology and pyrolysis at 600 °C [12]. The CO_2

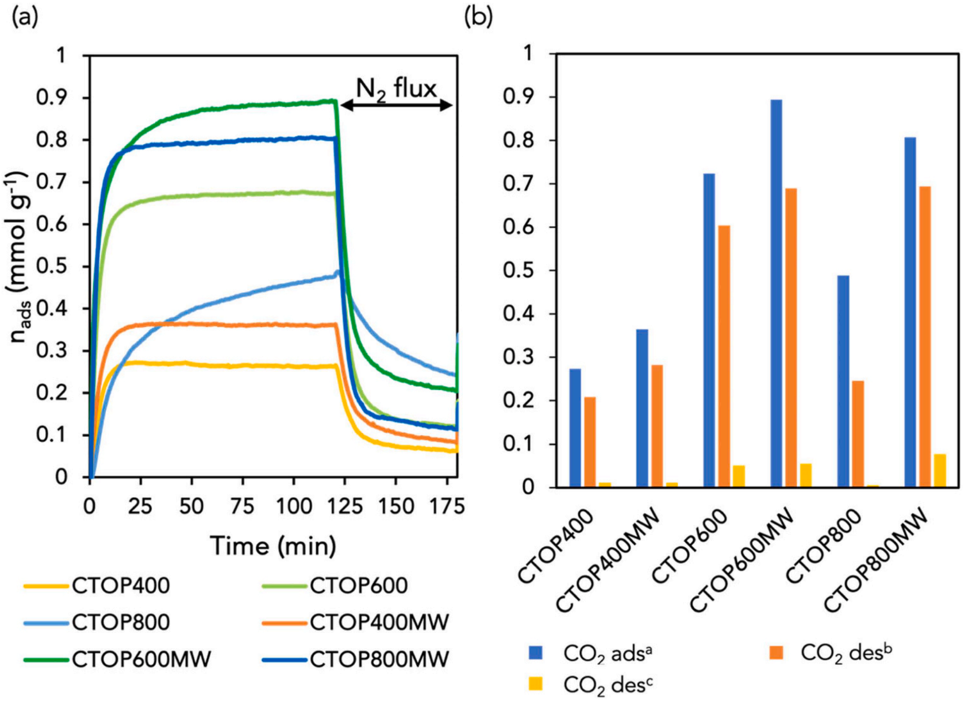

Fig. 2. (a) CO_2 adsorption kinetics under continuous flux of CO_2/N_2 gases (20 vol% of CO_2) at 35 °C and atmospheric pressure determined by TGA. Desorption was performed under 100 % N_2 flux. (b) Adsorption and desorption analysis of mixed CO_2/N_2 adsorption tests by TGA (^{a} Maximum CO_2 adsorption capacity in mmol g^{-1}; ^{b} CO_2 desorbed (mmol g^{-1}) after altering the gas mixture (20 vol% CO_2 in N_2) with a 100 vol% N_2 flux; and ^{c} CO_2 desorbed (mmol g^{-1}) after rise in temperature until 120 °C.

Table 2
Comparison of different biochar sorbents.

Feedstock (Sample)	T_P (°C)	S_{BET} (m^2g^{-1})	CO_2 uptake at 25 °C (mmol g^{-1})	N_2 uptake at 25 °C (mmol g^{-1})	CO_2/N_2 selectivity	REF
Sugarcane bagasse	600	388	1.36	-	-	[7]
Hickory wood	600	401	1.18	-	-	[7]
Chitosan	600	12	1.60	~0.20	~12	[12]
Pine sawdust	550	316	0.67	0.21	18	[18]
Paper mill sludge	600	86	~0.35	-	-	[18]
Anaerobic Digestion Digestate	600	13	1.02	-	-	[35]
CTOP600	600	263	1.43	0.03	334	This study
CTOP600MW	600	307	1.56	0.15	157	This study

uptake at 25 °C reached 1.60 mmol g^{-1} and the N_2 uptake at the same temperature was nearly 0.2 mmol g^{-1} with a selectivity rate of approximately 12 [12]. In another study, pine sawdust prepared in a muffle furnace at a heating rate of 7 °C/min for 2 h with no supply of air at 550 °C, exhibited 0.67 mmol g^{-1} of CO_2 capacity at 25 °C, 0.21 mmol g^{-1} for N_2 capacity at the same temperature with a CO_2/N_2 selectivity rate of 18.3 [18]. In the same study, paper mill sludge was prepared in the same conditions at 600 °C and obtained nearly 0.35 mmol g^{-1} of CO_2 adsorption capacity at 25 °C [18]. Lastly, in an interesting study, anaerobic digestion digestate was used as feedstock for the preparation of biochar by slow pyrolysis at 600 °C in a horizontal quartz tubular reactor under N_2 flow at a heating rate of 40 °C min^{-1} [18]. The biochar presented a CO_2 uptake at 25 °C of 1.02 mmol g^{-1} [18].

The CTOP600MW sample here reported demonstrated one of the highest CO_2 adsorption capacities (1.56 mmol g^{-1}) among the various biochars examined, albeit slightly lower than the sponge-like sorbent derived from chitosan in our prior research (1.60 mmol g^{-1}) [12]. Nevertheless, this biochar offers notable advantages in terms of time and energy efficiency compared to the sponge-like variant. It is produced in a single step through direct pyrolysis of chitosan powder, eliminating the need for chitosan dissolution, freezing, and freeze-drying. Additionally, the MW-assisted pyrolysis process for this sample takes just 20 min at 600 °C, significantly reducing both time and energy requirements for the pyrolysis stage. Moreover, most of the studies do not explore the N_2 adsorption capacity or the CO_2/N_2 selectivity of the materials. Besides showing a good amount of CO_2 adsorbed, CTOP600 and CTOP600MW samples also presented the highest CO_2/N_2 selectivity rates (334 and 157) than the reported materials [12,18]. These results conclude that the biochar sorbents prepared in this study show promising results in CO_2 adsorption capacity and CO_2/N_2 selectivity rate, especially the biochar prepared using the microwave-assisted heating method which yielded a higher CO_2 capacity (1.56 mmol g^{-1}) and high selectivity rate (157). As mentioned earlier, the microwave-assisted heating approach appears to be promising due to its shorter processing time and 13 % higher energy efficiency compared with the conventional furnace [35–37]. It may lead to substantial improvements in textural properties, enhancing CO_2 adsorption/desorption kinetics, as discussed in Section 3.1 and illustrated in Fig. 1(b).

3.3. *Investigating the influence of biochar microstructure on CO_2 adsorption*

To comprehend the primary adsorption mechanism on biochar adsorbents, various characterizations were conducted, including XPS, EA, TGA, SEM, XRD, and 77 K N_2 and 0 °C CO_2 adsorption-desorption isotherms. The functional groups present in the biochar sorbents were evaluated using XPS. The XPS analysis accurately determined the relative atomic concentration of elements on the sample surfaces, depicted

Table 3
Relative atomic concentration of biochar sorbents determined by XPS and EA and C1s and N1s core level assignments evaluated from deconvolution procedures.

	CTOP400	CTOP400MW	CTOP600	CTOP600MW	CTOP800	CTOP800MW
Relative atomic concentration (at%)						
C1s	77.5 (71.5)	76.5 (69.0)	74.4 (74.2)	63.5 (73.3)	77.9 (78.0)	69.7 (72.0)
O1s	12.4	12.3	12.8	22.9	14.9	23.4
N1s	8.6 (11.3)	9.4 (11.6)	9.5 (10.1)	9.4 (9.8)	4.5 (8.7)	3.9 (7.8)
Ca2p	1.5	0.4	2.6	3.7	1.8	3.0
Si2p	n.d.	0.7	0.4	n.d.	n.d.	n.d.
Cl2p	n.d.	0.7	0.2	0.2	n.d.	n.d.
S2p	n.d.	n.d.	0.1	0.3	0.5	n.d.
Na1s	n.d.	n.d.	n.d.	n.d.	0.4	n.d.
Carbon species (%)						
C-C/H	48.1	38.4	63.7	44.7	67.0	26.8
C-O-/N	26.4	33.8	16.7	21.3	9.0	29.2
O-C-O	13.7	15.8	6.5	13.1	11.7	23.7
C═O	6.6	5.5	3.4	9.7	3.4	7.0
$-CO_3^{2-}$	2.0	3.7	5.8	5.7	5.8	6.4
π-π*	3.2	2.8	3.9	5.5	3.1	6.9
Nitrogen species (%)						
Pyridinic	36.2	26.7	46.5	31.1	37.7	18.9
Amino group	7.2	21.5	16.8	12.5	14.5	25.0
Pyrrolic	27.2	31.4	30.5	37.2	19.8	31.2
Graphitic center	26.6	17.2	4.5	14.7	24.1	20.6
Graphitic valley/Pyridine-N-oxide	2.8	3.2	1.7	4.5	3.9	4.3

n.d. denotes for non-detected. The values in parentheses are obtained from the EA.

in Table 3, calculated from high-resolution spectra for a better determination, while survey scans (Figure S1) can clearly illustrate overall the presence of C, O, N, and Ca species in the biochar samples. The presence of Ca species was attributed to residual calcium carbonate from the chitosan commercial powder, potentially resulting from incomplete demineralization during chitin extraction from crustaceous shells.

Figure S1 shows an increase in the oxygen peak, as pyrolysis temperature rose, especially for MW samples, with CTOP400 and CTOP400MW exhibiting the lowest intensity and CTOP800MW showing the highest. Both XPS and elemental analysis (EA), reported in Table 3, indicated a slight increase in N content with temperature elevation from 400 to 600 °C, followed by a significant decline at 800 °C. The nitrogen content remained consistent between heating processes. EA data revealed that higher pyrolysis temperatures correlated with lower nitrogen content, a trend also evident in the spectra.

Fig. 3 and Table 3 illustrate deconvolution methods and relative percentages of chemical species. The analysis begins with the examination of the C1s core level peak (Fig. 3(a)) to ascertain the abundance of graphitic species and bonds involving oxygen and/or nitrogen atoms. Beyond the known chemical shifts due to C-C/C-H, shifts are observed due to C interactions with O and/or N (C-O/N), (O-C-O), (C═O), and $-CO_3^{2-}$ originating from residual calcium carbonate in chitosan.

The π-π* shake-up satellite, a characteristic feature of carbon's sp^2 hybridization, is marked by a decrease in C-O/N bonds peak intensity as the pyrolysis temperature increases, aligning with the reduction of N peaks intensity reported in the survey spectra (Figure S1 and Table 3). Furthermore, there is a noticeable trend of decreased intensity in peak associated with the C-O-/N bonds with rising temperature, suggesting enhanced carbonization of the samples. Additionally, the component of π-π* peak shows increased intensity with temperature, serving as another indicator of the graphitization process.

From the examination of the N1s core level peaks (Fig. 3(b)), the intensity of peak pyridinic-N increases as the temperature climbs from 400 to 600 °C but drops as it reaches 800 °C in the biochar samples. The same is observed for the peak attributed to pyrrolic-N. Intriguingly, at the same temperatures, samples pyrolyzed using microwave-assisted heating exhibit less pyridinic-N peak intensity than those pyrolyzed using conventional heating, although the opposite is observed for pyrrolic-N peak.

The thermal stability of the chitosan-based biochar samples was examined by TGA (Figure S2) to determine the ideal temperature for degassing the biochar sorbents while also preventing deterioration. All

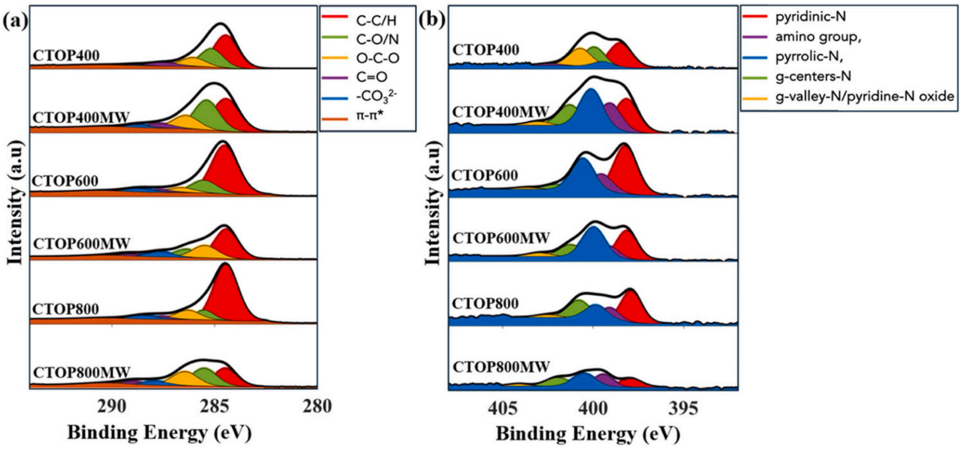

Fig. 3. (a) C1s HR spectra for all the biochar samples: *red* for C-C/H, *green* for C-O/N, *yellow* for O-C-O, *purple* for C═O, *blue* for $-CO_3^{2-}$ and *darker red* for π-π* transition; (b) N1s HR spectra for all the samples analyzed: *red* for pyridinic-N, *purple* for amino group, *blue* for pyrrolic-N, *green* for graphitic centers-N and *yellow* for graphitic valley-N or pyridine-N oxide bond.

samples present an initial weight loss of 5–12 % between 50 and 120 °C, which can be attributed to the desorption of water and other adsorbed gases, followed by a second weight loss of 82–90 % between 500 and 700 °C (or between 350 and 700 °C in the case of samples CTOP400 and CTOP400_MW) that can be correlated to the thermal degradation of the material [12]. The residual mass of the samples, which seems to be around 2–7 %, is mainly composed of inorganic compounds and ashes, which can only be removed at temperatures higher than 1200 °C. The increase in pyrolysis temperature has a significant impact on the thermal stability of the samples since those pyrolyzed at lower temperatures showed lower thermal stability compared to those pyrolyzed at higher temperatures [12]. Therefore, the materials' thermal stability is improved when the pyrolysis temperature is raised, as expected [38].

X-ray diffraction (XRD) analysis is performed to identify crystallographic phases in the biochar samples. Figure S3 shows that the biochars prepared are amorphous solids. The peaks located at $2\theta = 20$–30 ° (graphite 002) evidence the stacking structure of aromatic layers [39]. The XRD of the chitosan powder was also performed and three distinct crystallographic reflections were observed at $2\theta = 10$, 20, and 30 ° related to chitosan, which were also previously documented in the literature [40]. The presence of calcium carbonate ($CaCO_3$) on the chitosan commercial powder was confirmed by observation of five peaks, ascribed to crystalline calcite phases ($2\theta = 29$, 39, 43, 47, and 58 °), [41] which appear to be present in the biochar samples as well, as suggested by the XPS results (Table 3 and Fig. 3). In addition, vaterite or aragonite crystalline phases could be the source of further unexplained peaks [41].

The textural features and porosity of the materials were examined using SEM and N_2 adsorption/desorption isotherms at −196 °C. The SEM images of all the biochar samples are shown in Fig. 4 and S4, giving a visual understanding of the morphological traits of the pyrolyzed biochar. The images show that the samples obtained from both heating procedures and temperatures exhibit heterogeneity in particle size and form. The biochar materials exhibit rough surfaces and obvious signs of macroporosity. One interesting finding is that conventional heating seems to produce biochar that is denser than microwave heating, which can limit the material's ability to adsorb CO_2 molecules. Interestingly, for the biochar samples pyrolyzed using the microwave method, raising the temperature from 400 to 600 °C causes a noticeable increase in porosity (Figure S4, panels d–e), which is also apparent when contrasting the images from the two heating methods of the samples pyrolyzed at 600 °C (Fig. 4).

From observing Fig. 5(a), which displays N_2 sorption isotherms (at −196 °C) for the biochar sorbents prepared through MW-assisted pyrolysis, it can be confirmed that, for the samples CTOP600MW and CTOP800MW, the N_2 sorption isotherms are type I curves, which are generally seen for microporous materials. At the bottom of the graph, the isotherm for the sample CTOP400MW indicates minimal or negligible N_2 adsorption at −196 °C. The samples from conventional-assisted heating have the same behavior as the CTOP400MW material. This sort of sample frequently exhibits this restricted N_2 adsorption capacity at cryogenic temperatures, which is primarily caused by the predominance of ultra-micropores in their porous structure [42].

Nevertheless, the conventional surface area and pore size distribution (PSD) curves for biochars might not be correctly predicted by N_2 adsorption-desorption isotherms [43], as this type of adsorbent mainly display micropores. Density functional theory (DFT) computation can be used to get a more accurate description of the microporosity of biochars and the pore size of microporous carbons (porous with a pore size below 2 nm) can be determined using CO_2 adsorption at 0 °C [44]. Similar approaches have been used in earlier studies to characterize diverse activated carbons using the adsorption isotherms of different gases and models like the nonlocal density functional theory (NLDFT) and grand canonical Monte Carlo (GCMC) [45].

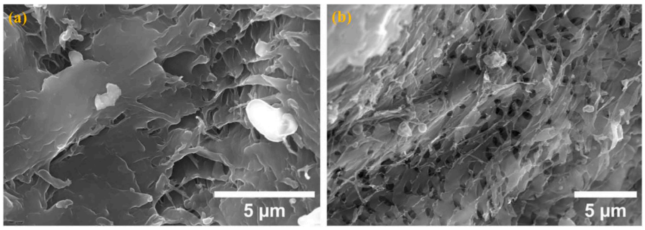

Fig. 4. SEM micrographs of the biochar samples pyrolyzed at 600 °C from both heating methods (a - CTOP600 and b - CTOP600_MW).

For those reasons, the NLDFT and MC models were used to determine the PSD curves and pore volume of the biochar sorbents. The specific surface area (S_{BET}) is determined by applying the theory proposed by Brunauer-Emmett-Teller (BET). The textural properties of the samples derived from CO_2 adsorption at 0 °C are summarized in Table 4. The results from both heating methods indicate that when raising the pyrolysis temperature from 400 to 600 °C there is an enhancement in S_{BET}, that slightly reduces as the temperature is increased to 800 °C. The inferior CO_2 adsorption capacity observed for sample CTOP800 (see Fig. 1(a)) can be due to its reduced nitrogen content observed by EA (Table 3) which directly translates to lower CO_2 uptake [46]. The low S_{BET} and V_P of this sample also sustain this hypothesis. Notably, the biochar samples prepared using the microwave heating method exhibit a higher S_{BET} than those prepared using a conventional furnace, with the CTOP600MW having the highest value overall of 307 $m^2\ g^{-1}$. Regarding pore volume calculations derived from the NLDFT method, similar trends are observed. These samples' high S_{BET} and V_P could be an explanation for the higher CO_2 adsorption capacity. The material that possessed the highest pore volume value was CTOP600MW (V_P = 0.139 $cm^3\ g^{-1}$). This material's high S_{BET} and high pore volume might be one of the reasons behind its high CO_2 adsorption capacity illustrated in Fig. 1(a).

The PSD curves (Fig. 5(b)) obtained by employing the NLDFT method displayed pore widths ranging from 0.34 to 0.70 nm for both pyrolysis processes, thus confirming the presence of ultra- and microporosity in all biochar samples with the higher ultra- and micropore population corresponding to the materials prepared using microwave-assisted pyrolysis. This fact could justify the improved adsorption capacity of this set of samples. From the PSD curves, one can conclude that for the chitosan-derived sorbents, most of the pores are ultra-micropores with sizes of about ≈ 0.35 and 0.5 nm. The decline of the CO_2 adsorption capacity of the sample CTOP800 could be explained by the pore shrinkage resulting from the increase in pyrolysis temperature from 600 to 800 °C, hampering the CO_2 molecule diffusion into the pores. While this is not the case for microwave-treated samples (CTOP600MW and CTOP800MW) where the generated microporosity provides the highest selectivity of these samples towards CO_2 (Fig. 1(b)) as well as their fast adsorption/desorption kinetics (Fig. 2(a)).

Fig. 6 shows the enthalpy of adsorption (ΔH_{ads}) values for the MW-pyrolyzed samples. A high ΔH_{ads} indicates a strong affinity between the adsorbent and the adsorbate [32]. There is an increase in ΔH_{ads} when the pyrolysis temperature is raised from 400 to 600 °C, followed by a drop at 800 °C. Energy heterogeneity is indicated by the initial decreasing trend in the results with the amount of CO_2 adsorbed (from 44–57 $kJ\ mol^{-1}$ to 28–43 $kJ\ mol^{-1}$). For chemisorption, ΔH_{ads} values typically fall between 60 and 90 $kJ\ mol^{-1}$, while for physisorption, they typically fall between 25 and 50 $kJ\ mol^{-1}$ [47]. Considering these findings, it appears that physisorption may be the primary adsorption mechanism. The CO_2 isosteric heats of adsorption are consistent with those reported for other biochars obtained by the slow pyrolysis method [7]. Furthermore, these values fall within the engineering-recommended range for post-combustion capture (30–60 $kJ\ mol^{-1}$) [48]. The results of isosteric enthalpy of adsorption calculations for the biochar obtained through conventional pyrolysis are presented in Figure S5 and display a similar pattern apart from CTOP400.

To assess the impact of nitrogen content while excluding the effects

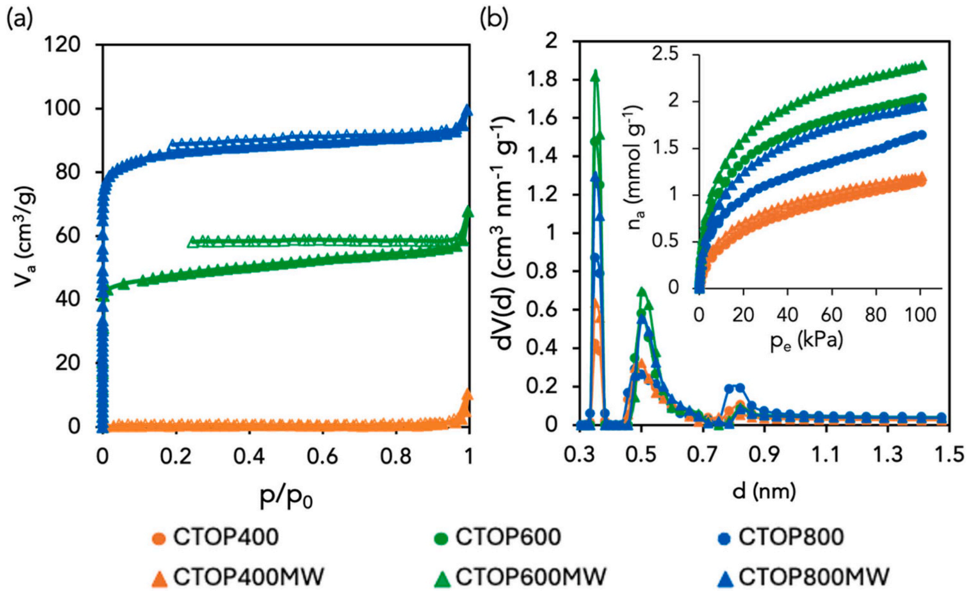

Fig. 5. (a) Adsorption-desorption isotherms of N_2 at −196 °C of all the biochar sorbents (filled symbol – adsorption; empty symbol – desorption). The desorption branch of CTOP600MW is not in equilibrium; (b) PSD curves determined using the NLDFT method applied to the CO_2 adsorption isotherms at 0 °C (inset).

Table 4
Textural properties of the chitosan-based biochar samples determined from the CO_2 adsorption isotherms at 0 °C.

Sample	$S_{BET\text{-}micro}$ (m^2 g^{-1})[a]	$V_{P\text{-}NLDFT}$ (cm^3 g^{-1})[b]	$V_{P\text{-}MC}$ (cm^3 g^{-1})[c]	d_p (nm)
CTOP400	158	0.078	0.073	0.31 – 1.47
CTOP400MW	164	0.076	0.074	0.35 – 1.47
CTOP600	263	0.119	0.104	0.35 – 1.47
CTOP600MW	307	0.139	0.124	0.35 – 1.47
CTOP800	186	0.112	0.116	0.31 – 1.47
CTOP800MW	258	0.119	0.107	0.35 – 1.47

[a] BET specific surface area - correlation coefficient (R^2)=[0.994–0.998];
[b] $V_{P\text{-}NLDFT}$ denotes pore volume determined from CO_2 adsorption isotherms at 0 °C and applying the NLDFT method – Fitting error (%) = [2.00–5.90];
[c] $V_{P\text{-}MC}$ denotes pore volume determined from CO_2 adsorption isotherms at 0 °C and applying the MC method - Fitting error (%) = [0.29–1.41].

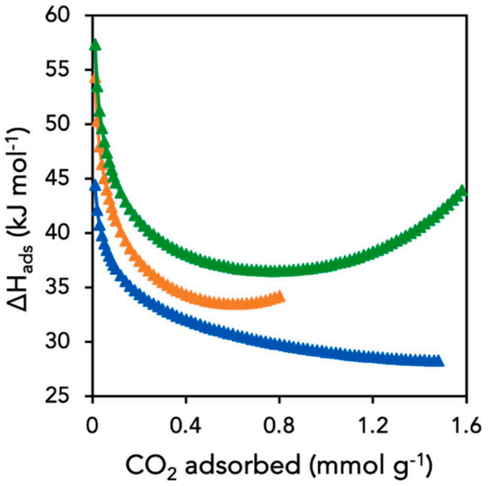

Fig. 6. Isosteric enthalpy of adsorption for CO_2 calculated via the Clausius–Clapeyron approach with the Freundlich-Langmuir coefficients estimated from the isotherms at 0 and 25 °C for the biochar samples prepared with microwave-assisted pyrolysis (orange- 400 °C; Green - 600 °C; blue - 800 °C).

of microporosity, the CO_2 adsorption amount was normalized by the micropore volume determined by the MC method (CO_2 ads/V_{micro}, mmol cm^{-3}), and the results were correlated with the nitrogen content determined by elemental analysis (Fig. 7). The experimental data were fitted with a linear function for biochars prepared using microwave-assisted pyrolysis (panel (a)) and conventional pyrolysis (panel (b)). For the microwave-assisted biochars, an increase in CO_2 adsorption capacity was observed with higher nitrogen content. In contrast, the opposite trend was noted for biochars obtained via conventional pyrolysis. This difference could be related to the presence of macroporosity in the former samples, which might enhance the diffusion of CO_2 molecules into the micropores, allowing them to interact with nitrogen species on the material's surface. The contribution of each nitrogen species in CO_2 adsorption was estimated from the slope of the trend line, based on the XPS data (Table 3) of the microwave-derived biochars. Most nitrogen species observed, apart from pyridinic N, appear to enhance CO_2 adsorption to varying degrees (Fig. 7, panels (c)-(g)). Among these, graphitic valley-N/ pyridinic-N-oxide significantly increases CO_2 adsorption, as indicated by the comparison of slope values. This result is in agreement with our previous findings [12].

3.4. 3D-printed biochar adsorbent

The ability of the sorbent to be used in large-scale industrial applications can be increased by immobilizing the sorbent's particles onto a solid support or within a matrix. This can also help to avoid problems such as dusting, sorbent material loss, and problems with fluidization and pressure drop [48,49]. Additionally, immobilizing porous sorbents can boost process efficiency and scalability, increase stability, handling, and separation, and improve recyclability, reusability, and mass transfer kinetics [50]. Inorganic polymers (IPs, also known as geopolymers) are amorphous aluminosilicate materials, defined by a three-dimensional network with structural mesoporosity, which have been investigated for environmental applications, namely dyes [29] and metals [51] adsorption from water but also for CO_2 capture [51–53]. Besides the cost-effectiveness and low carbon footprint, due to the limited energy

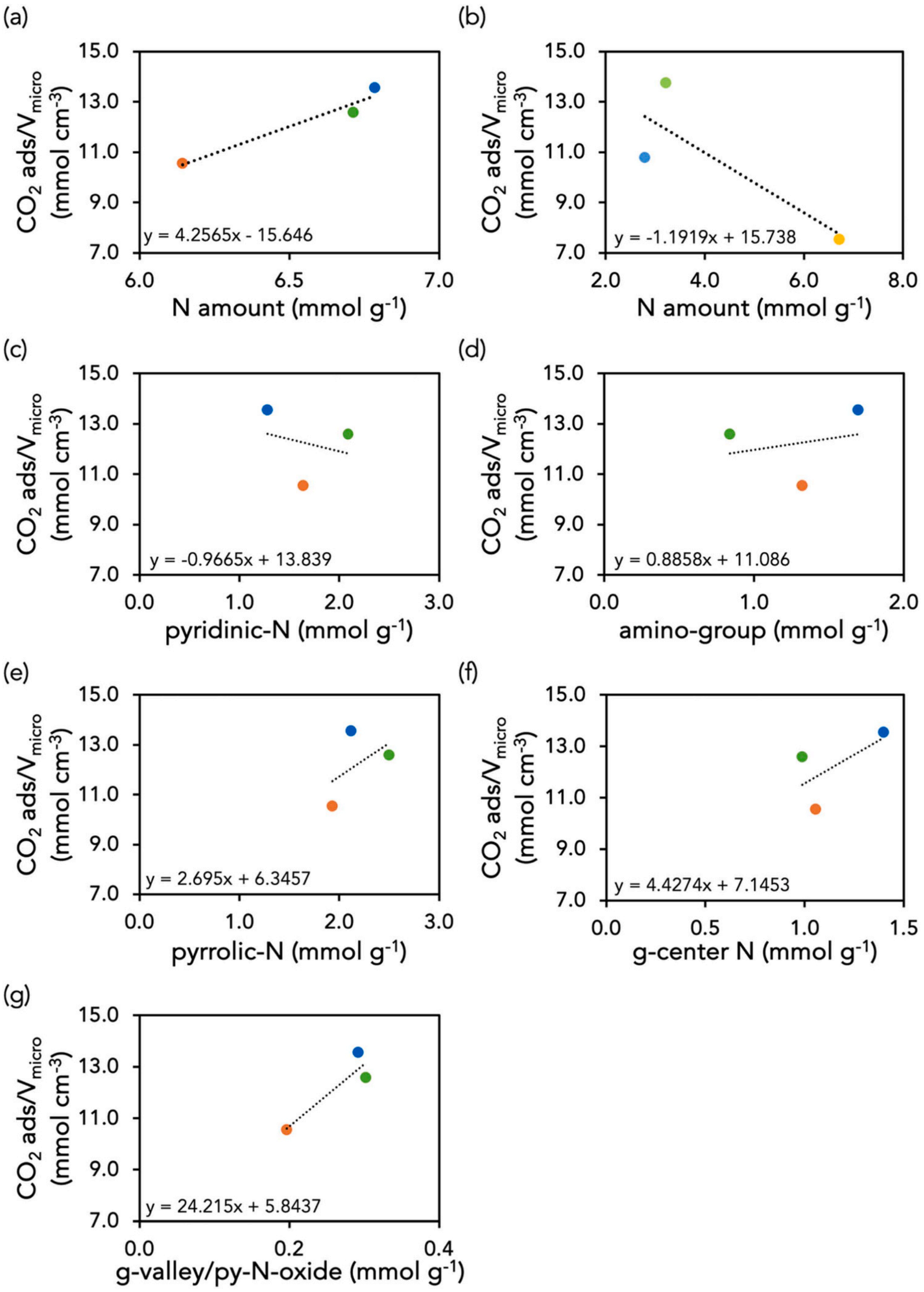

Fig. 7. CO_2 normalized adsorption *vs* nitrogen content (panel (a) – microwave-assisted pyrolysis; panel (b) – conventional-assisted pyrolysis) and type of N-species (panels (c) to (g)) on the biochars produced through microwave-assisted pyrolysis. g- denotes graphitic and py- denotes pyridinic. Color scheme shown in Fig. 2 - pyrolysis at 400 (orange color), 600 (green color), and 800 °C (blue color).

consumption during the manufacturing process, geopolymers offer the advantage of allowing the incorporation of industrial-relevant residues such as red mud or fly ash [54–57], reducing the need for commercial virgin raw material (MK), aligned with principles of circular economy. In a recent study, we developed a method for preparing 3D-printed IPs containing 50 wt% of RM, thereby reducing MK usage, and successfully immobilizing the hazardous residue [29]. The preparation of biochar/inorganic polymer composites through additive manufacturing, namely DIW, is of interest as it allows to obtaining precisely designed structures with controlled size and shape, open microporosity, and interconnectivity between pores. Thus, this study also investigated the feasibility of preparing a 3D-printing biochar-containing adsorbent, by incorporating the best-performing biochar (CTOP600_MW) into IPs obtained by blending red mud (an alkaline hazardous by-product from the alumina industry) and metakaolin (the benchmark aluminosilicate raw material) with an alkaline activator solution (see Section 2.3.1).

3.4.1. Analysis of structural properties

High-resolution photographies from the optical microscope of the 3D-printed lattices depicted in Fig. 8 evidence ordered organization with controlled distance between filaments (300 ± 10 μm), which retained circular diameter (410 ± 10 μm), suggesting the optimum rheological properties of the optimized formulations. A comparison of Fig. 8(b) and (c), which depict the pristine material (3D-RM/MK) and the material incorporating biochar (3D-B/RM/MK), respectively, suggests an agglomeration of the biochar particles as evidenced by the presence of

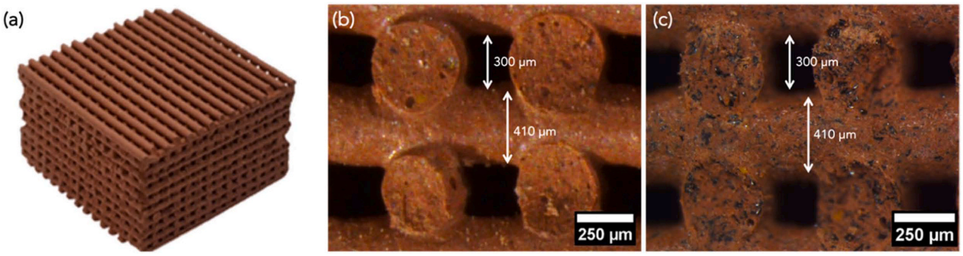

Fig. 8. High-resolution photographies of the 3D-printed structures without (panels (a) and (b)) and containing biochar (c).

irregular black spots in the biochar-incorporated material. This phenomenon can be explained by the hydrophobic nature of biochar, leading to agglomeration when exposed to water during the ink preparation step for the DIW process.

SEM micrographs of biochar-containing lattice presented in Fig. 9 panels (b) and (d) evidence significantly rougher surface texture of the filaments compared with the smooth surface of the biochar-free structure (Fig. 9 panels (a) and (c)). This difference is likely attributed to the presence of aggregated biochar particles protruding from the filament surface. Interestingly, the incorporation of biochar profoundly influences the filament interior, as evidenced by the presence of numerous pores. This contrasts distinctly with the counterpart material devoid of biochar, which exhibits a primarily dense structure with sparse pores. The presence of pores in the biochar-containing filaments can be attributed to the non-reactive nature of biochar, which disrupts the polymerization process and creates voids within the filament structure. This disruption is likely caused by the biochar's ability to act as a nucleating site for air bubbles, which further contribute to the porosity of the material. EDS maps of the printed lattices presented in Fig. 9 panels (e) – (j) confirmed the uneven distribution of carbon, showing distinct spots of agglomeration contrasting with the homogeneous distribution of Al, Si, and Fe derived from the IPs network.

The crystalline phases in the 3D-printed samples were identified by XRD [29], as shown in Figure S6. The 3D-RM/MK sample contains hematite (Fe_2O_3) and phases of hydroxide containing Al, such as boehmite (γ-AlO(OH)), chantalite ($CaAl_2SiO_4(OH)_4$), and gibbsite (α-Al(OH)$_3$). Also, the TiO_2 phases (rutile and anatase), and sodium aluminum carbonate silicate ($Na_5AlCSiO_3O_{15}$) are present, which is in agreement with the chemical composition of the solid raw materials (Table S1) and crystalline phases previously reported for these materials [29]. These crystalline phases are also present in the carbon-containing structure besides two unidentified peaks at $2\theta = 34\,^\circ$ sourced from the biochar sample. Also, the calcite phase at $2\theta = 29\,^\circ$ (see Figure S3) from calcium carbonate content present in the biochar sample was corroborated by XPS results (Fig. 3 and S1, and Table 3).

The chemical composition of 3D-printed samples was investigated by FTIR spectroscopy and EA analysis. As demonstrated in Figure S7, the FTIR spectra of the carbon-containing structures reveal bands matching those present in the analogous biochar-free sample. It was possible to identify the asymmetric band, with a maximum at about 3450 cm^{-1}, and at around 1640 cm^{-1} characteristic of the adsorbed water molecules. The peak at 1450 cm^{-1} is related to stretching vibrations of O-C-O bonds resulting from carbonation and the asymmetries of Si-O-Si/Si-O-Al in the polymeric network are shown by the peak at 980 cm^{-1} [29]. The chemical composition determined by EA presented in Table S4, demonstrates that the incorporation of biochar significantly increased the C and N content from 0.79 % to 10.41 % and 0.07 to 1.29 %, respectively.

3.4.2. CO_2 adsorption

Fig. 10 (a) shows the pure CO_2 and N_2 adsorption isotherms at 25 °C for 3D-printed adsorbents as previously observed for the biochar materials, the adsorption of CO_2 is consistently higher than that of N_2, indicating a strong potential for separating CO_2 from N_2. By comparing the biochar-containing adsorbent with the counterpart material without biochar (3D-RM/MK), it is possible to determine that adding biochar greatly increased the IPs adsorbent's capacity and affinity for CO_2 with a 4-fold increase. This is supported by the Henry constants (K_H) and Virial coefficients (C_1, C_2, and C_3) for the adsorption by applying the Virial model, presented in Table S5. Determining Henry constants for N_2 proved unattainable for any of the materials, primarily due to their minimal adsorption capacity for this gas. Similarly, the IAST selectivity assessment was not possible for these materials since most of the parameters could not be determined due to negligible amounts of N_2 adsorbed or due to constraints in the fitting of the results. Nevertheless, all the parameters from the Freundlich-Langmuir fitting are summarized in Table S6. This suggests that the prepared samples exhibit a high degree of selectivity for separating these two gases. Results also show that

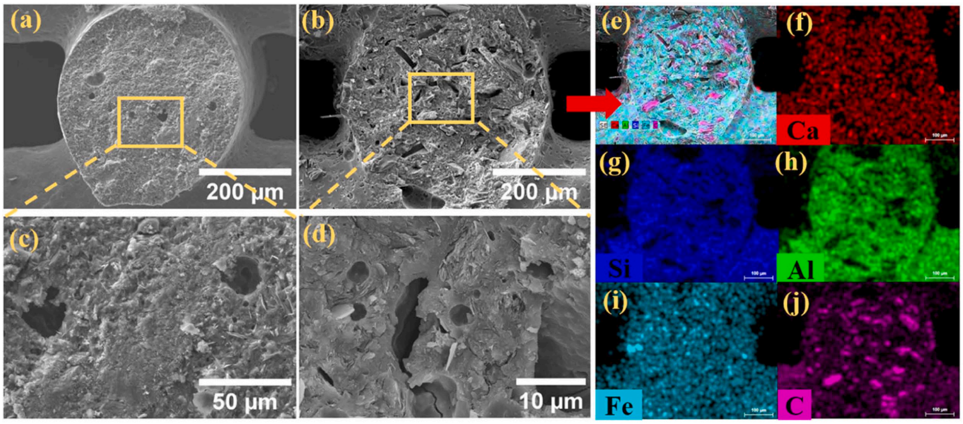

Fig. 9. SEM micrographs of the 3D-printed structures without (panels a and c) and containing biochar (panels b and d) and EDS maps of the biochar-containing 3D-printed sample (3D-B/RM/MK) (panels e - j).

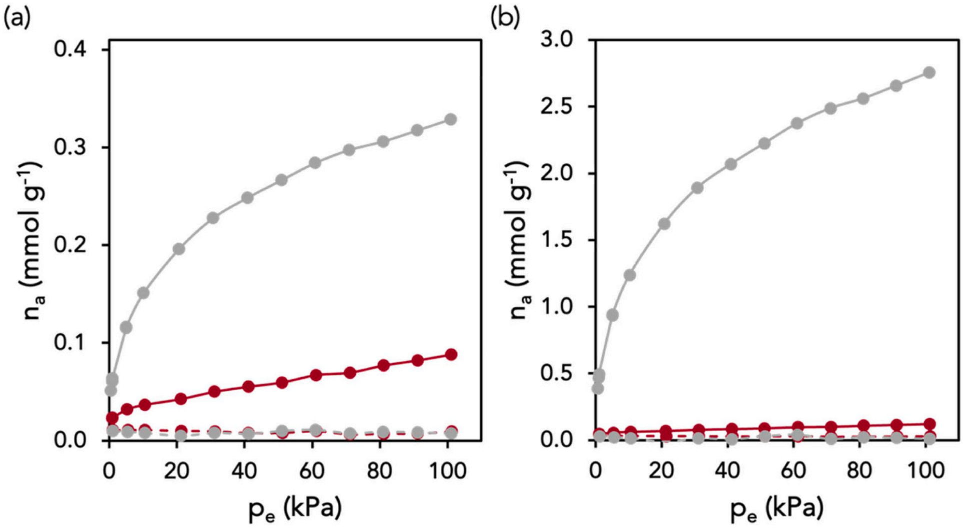

Fig. 10. a) Adsorption isotherms of pure CO_2 (circle symbols with solid lines) and N_2 (circle symbols with dashed lines) gases at 25 °C of the 3D-printed materials (gray – 3D-B/RM/MK; dark red – 3D-RM/MK). b) CO_2 and N_2 adsorption isotherms of the 3D-printed materials normalized per unit mass of incorporated carbonaceous material.

the CO_2 adsorption capacity of the biochar-containing sorbent reached 0.32 mmol g^{-1}, this being roughly four times lower than the value observed for the biochar sample (see details in Fig. 1(a)). However, it should be noted that the biochar incorporation in the bulk-type structure corresponded to only 20 wt% of the solids. When considering this, the results suggest that the efficiency of the biochar in the composites was mostly preserved despite the agglomeration phenomenon (see Fig. 9). To ascertain whether the CO_2 adsorption capacity of the biochar is impacted upon its incorporation into the 3D-printed composite, the quantities of adsorbed gases were normalized per unit mass of incorporated carbonaceous material (derived from the carbon and nitrogen quantities obtained via EA, Table 3). This normalization accounts for the potential effect of a high portion of RM/MK which may diminish CO_2 adsorption. Fig. 10 (b) demonstrates an increase from the original carbonaceous powder to the corresponding 3D-printed composite, indicating a potential synergy between the carbon and other components within the printed material to enhance CO_2 adsorption. This suggests that developing a denser network of micropores within the 3D-printed materials might be responsible for this enhancement. These promising results indicate the technical feasibility of this innovative approach, incorporating biochar into inorganic polymers, which could potentially pave the way towards the development of efficient bulk-type CO_2 sorbents.

Table 5 offers a synopsis of the textural attributes of the 3D-printed materials as determined by N_2 adsorption at 77 K. The pore volume data from the MC model is presented in Table S7. By observing the pore volume resulting from the inclusion of biochar ($V_P = 0.030$ cm^3 g^{-1}) we can see that this value nearly tripled when compared to the pore volume from the reference sorbent ($V_P = 0.009$ cm^3 g^{-1}).

The pore size distribution curves determined from the adsorption of CO_2 at 0 °C for the 3D-printed structures predominantly highlight pore diameters within the 0.35 – 0.85 nm range (micropore size), with the biochar-incorporated structure exhibiting a higher density of pores in that specific range (Figure S8). In contrast, the PSD curve of the sample 3D-RM/MK indicates a lower number of pores across the displayed range, suggesting its lower porosity compared to structures containing biochar. The inclusion of biochar is believed to contribute to the increased porosity. This observation is further supported by the diminished capacity to adsorb CO_2 from the reference sample, even at lower temperatures (0 °C), as illustrated in Figure S8 (inset). The uptake of CO_2 in both samples decreases as the adsorption temperature increases, ranging from 0 to 25 °C. This suggests that the predominant process is physisorption.

Table 5
Textural properties of the 3D-printed materials from N_2 adsorption at 77 K.

Sample	S_{BET} (m^2 g^{-1})	V_P (cm^3 g^{-1})
3D-RM/MK	50	0.009
3D-B/RM/MK	49	0.030

The ΔH_{ads} of the 3D-B/RM/MK material was determined with a value of 20 kJ mol^{-1} (Figure S9), confirming physisorption as the predominant adsorption mechanism. These values fall close to the 30–60 kJ mol^{-1} post-combustion capture range, as advised by engineering [48].

4. Conclusions

Chitosan-derived biochar sorbents were prepared at different temperatures using conventional and microwave pyrolysis heating to evaluate their textural properties and CO_2/N_2 adsorption-separation behavior.

The MW-assisted method approach stood out, yielding sorbents with high CO_2 adsorption capacity, selectivity, and fast adsorption/desorption kinetics, while also being less time- and energy-consuming. These enhancements were related to increased N content (as observed by XPS and EA), higher surface area and pore volume, along with a combination of ultra-microporosity and macroporosity (as observed by adsorption isotherms and SEM images), facilitating better CO_2 interaction and adsorption/desorption performance. Combined with their typical stability in the presence of moisture (not evaluated in this study), these features are relevant for applications in direct air capture and flue gas treatment.

The biochar sample CTOP600MW emerged as the most effective, showing the highest CO_2 adsorption capacity at 25 °C and 1 bar (1.56 mmol g^{-1}). It demonstrated notable selectivity, as evidenced by both the IAST model (46.5 at 100 kPa) in a gas mixture comprising 20 % CO_2 and 80 % N_2 molar fraction and the adsorption isotherm under a continuous flux of a CO_2/N_2 gas mixture replicating the aforementioned conditions.

This sample was incorporated into a waste-based mixture (RM/MK) to create 3D-printed adsorbents, which exhibited higher CO_2 adsorption than N_2 at 25 °C and up to 1 bar, indicating selective CO_2 affinity. Incorporating 20 wt% of biochar into the 3D-RM/MK matrix resulted in a 4-fold increase in CO_2 adsorption capacity (1 bar and 25 °C), compared to the biochar-free sample (3D-RM/MK). Interestingly, the biochar incorporation did not lead to a similar improvement in N_2 adsorption. This enhanced performance, predicted by the IAST model, is attributed to increased microporosity.

Our study demonstrated the creation of highly selective biochars for CO_2/N_2 adsorption-separation through MW-assisted pyrolysis and their successful integration into a 3D-printed composite, contributing to waste valorization. Future investigations should explore higher biochar content in the 3D-printed matrix, alternative IPs raw materials, and performance under industrial conditions.

CRediT authorship contribution statement

Sergio Bocchini: Methodology, Investigation. **Micaela Castellino:** Writing – original draft, Methodology, Investigation, Data curation. **Rui M. Novais:** Writing – review & editing, Funding acquisition. **Nuno P.F. Gonçalves:** Writing – review & editing, Writing – original draft, Supervision, Methodology, Investigation, Funding acquisition, Data curation, Conceptualization. **Luís Mafra:** Writing – review & editing, Funding acquisition. **Mirtha A. O. Lourenço:** Writing – review & editing, Writing – original draft, Supervision, Methodology, Investigation, Funding acquisition, Data curation, Conceptualization. **Marina Ilkaeva:** Writing – review & editing, Methodology, Investigation, Data curation. **Inês Correia:** Writing – original draft, Methodology, Investigation, Data curation.

Declaration of Competing Interest

The authors declare that they have no known competing financial interests or personal relationships that could have appeared to influence the work reported in this paper.

Data availability

Data will be made available on request.

Acknowledgments

This work was developed within the scope of the project CICECO-Aveiro Institute of Materials, UIDB/50011/2020 (DOI 10.54499/UIDB/50011/2020), UIDP/50011/2020 (DOI 10.54499/UIDP/50011/2020) & LA/P/0006/2020 (DOI 10.54499/LA/P/0006/2020), financed by national funds through the FCT/MCTES (PIDDAC). This work has received funding from the European Research Council (ERC) under the European Union's Horizon 2020 Research and Innovation Program (Grant Agreement 865974). FCT is also acknowledged by M.I. and M.A.O.L. for Researcher positions (CEECIND/00546/2018 and CEECIND/01158/2021 (DOI: 10.54499/2021.01158.CEECIND/CP1659/CT0022), respectively). M.I. also acknowledges the Spanish Ministry of Science, Innovation and Universities for the "Beatriz Galindo" Scholarship (MU-23-BG22/00145). N.G. and M.A.O.L acknowledge the funding from the European Union's Horizon Europe research and innovation program under the Marie Skłodowska-Curie Actions PF grant agreement No 101065059 and ERA-PF grant agreement No 101090287. R.N. would like to thank FCT project MAXIMUM (PTDC-CTM-CTM-2205–2020, DOI 10.54499/PTDC/CTM-CTM/2205/2020).

Appendix A. Supporting information

Supplementary data associated with this article can be found in the online version at doi:10.1016/j.jece.2024.113875.

References

[1] A.N. Shafawi, A.R. Mohamed, P. Lahijani, M. Mohammadi, Recent advances in developing engineered biochar for CO2 capture: an insight into the biochar modification approaches, J. Environ. Chem. Eng. 9 (6) (2021) 106869, https://doi.org/10.1016/j.jece.2021.106869.

[2] Y. Li, G. Ruan, A.S. Jalilov, Y.R. Tarkunde, H. Fei, J.M. Tour, Biochar as a renewable source for high-performance CO2 sorbent, Carbon 107 (2016) 344–351, https://doi.org/10.1016/j.carbon.2016.06.010.

[3] S. Choi, J.H. Drese, C.W. Jones, Adsorbent materials for carbon dioxide capture from large anthropogenic point sources, ChemSusChem 2 (9) (2009) 796–854, https://doi.org/10.1002/cssc.200900036.

[4] B.P. Spigarelli, S.K. Kawatra, Opportunities and challenges in carbon dioxide capture, J. CO2 Util. 1 (2013) 69–87, https://doi.org/10.1016/j.jcou.2013.03.002.

[5] M.A.O. Lourenço, C. Nunes, J.R.B. Gomes, J. Pires, M.L. Pinto, P. Ferreira, Pyrolyzed chitosan-based materials for CO2/CH4 separation, Chem. Eng. J. 362 (2019) 364–374, https://doi.org/10.1016/j.cej.2018.12.180.

[6] G.K. Parshetti, S. Chowdhury, R. Balasubramanian, Biomass derived low-cost microporous adsorbents for efficient CO 2 capture, Fuel 148 (2015) 246–254, https://doi.org/10.1016/j.fuel.2015.01.032.

[7] A.E. Creamer, B. Gao, M. Zhang, Carbon dioxide capture using biochar produced from sugarcane bagasse and hickory wood, Chem. Eng. J. 249 (2014) 174–179, https://doi.org/10.1016/j.cej.2014.03.105.

[8] U. Kamran, S.-J. Park, Chemically modified carbonaceous adsorbents for enhanced CO2 capture: a review, J. Clean. Prod. 290 (2021) 125776, https://doi.org/10.1016/j.jclepro.2020.125776.

[9] X. Wang, C. Song, Carbon capture from flue gas and the atmosphere: a perspective, Front. Energy Res. 8 (2020), https://doi.org/10.3389/fenrg.2020.560849.

[10] M.A.O. Lourenço, M. Fontana, P. Jagdale, C.F. Pirri, S. Bocchini, Improved CO2 adsorption properties through amine functionalization of multi-walled carbon nanotubes, Chem. Eng. J. 414 (2021), https://doi.org/10.1016/j.cej.2021.128763.

[11] A.I. Osman, M. Hefny, M.I.A. Abdel Maksoud, A.M. Elgarahy, D.W. Rooney, Recent advances in carbon capture storage and utilisation technologies: a review, Environ. Chem. Lett. 19 (2021) 797–849, https://doi.org/10.1007/s10311-020-01133-3.

[12] M.A.O. Lourenço, T. Frade, M. Bordonhos, M. Castellino, M.L. Pinto, S. Bocchini, N-doped sponge-like biochar: A promising CO2 sorbent for CO_2/CH_4 and CO2/N_2 gas separation, Chem. Eng. J. 470 (2023), https://doi.org/10.1016/j.cej.2023.144005.

[13] Y. Qiao, C. Wu, Nitrogen enriched biochar used as CO2 adsorbents: a brief review, Carbon Capture Sci. Technol. 2 (2022), https://doi.org/10.1016/j.ccst.2021.100018.

[14] H. Zhang, Z. Yu, Q. Huang, A review: utilization of biochar for wastewater treatment. Application of Adsorbents for Water Pollution Control, BENTHAM SCIENCE PUBLISHERS, 2012, pp. 413–431, https://doi.org/10.2174/978160805269111201010413.

[15] P.D. Dissanayake, et al., Biochar-based adsorbents for carbon dioxide capture: a critical review, Renew. Sustain. Energy Rev. 119 (2020), https://doi.org/10.1016/j.rser.2019.109582.

[16] P.D. Dissanayake, et al., Biochar-based adsorbents for carbon dioxide capture: a critical review, Renew. Sustain. Energy Rev. 119 (2020) 109582, https://doi.org/10.1016/j.rser.2019.109582.

[17] Y. Qiao, C. Wu, Nitrogen enriched biochar used as CO2 adsorbents: a brief review, Carbon Capture Sci. Technol. 2 (2022) 100018, https://doi.org/10.1016/j.ccst.2021.100018.

[18] A.D. Igalavithana, et al., Carbon dioxide capture in biochar produced from pine sawdust and paper mill sludge: effect of porous structure and surface chemistry, Sci. Total Environ. 739 (2020) 139845, https://doi.org/10.1016/j.scitotenv.2020.139845.

[19] C. Yang, T. Zhao, H. Pan, F. Liu, J. Cao, Q. Lin, Facile preparation of N-doped porous carbon from chitosan and NaNH2 for CO2 adsorption and conversion, Chem. Eng. J. 432 (2022) 134347, https://doi.org/10.1016/j.cej.2021.134347.

[20] S. Fan, et al., Value-added biochar production from microwave pyrolysis of peanut shell, Int. J. Chem. React. Eng. 21 (8) (2023) 1035–1046, https://doi.org/10.1515/ijcre-2023-0005.

[21] J. Li, et al., Biochar from microwave pyrolysis of biomass: a review, Biomass Bioenergy 94 (2016) 228–244, https://doi.org/10.1016/j.biombioe.2016.09.010.

[22] Y. Zhang, S. Fan, T. Liu, W. Fu, B. Li, A review of biochar prepared by microwave-assisted pyrolysis of organic wastes, Sustain. Energy Technol. Assess. 50 (2022) 101873, https://doi.org/10.1016/j.seta.2021.101873.

[23] S. Ethaib, R. Omar, S.M.M. Kamal, D.R. Awang Biak, S.L. Zubaidi, Microwave-assisted pyrolysis of biomass waste: a mini review, Processes 8 (9) (2020) 1190, https://doi.org/10.3390/pr8091190.

[24] M.J. Gronnow, et al., Torrefaction/biochar production by microwave and conventional slow pyrolysis – comparison of energy properties, GCB Bioenergy 5 (2) (2013) 144–152, https://doi.org/10.1111/gcbb.12021.

[25] Z. Bi, B.B. He, Biochar from microalgae. 3rd Generation Biofuels, Elsevier, 2022, pp. 613–637, https://doi.org/10.1016/B978-0-323-90971-6.00025-5.

[26] V. Kurian, M. Gill, B. Dhakal, A. Kumar, Recent trends in the pyrolysis and gasification of lignocellulosic biomass. Biofuels and Bioenergy, Elsevier, 2022, pp. 511–552, https://doi.org/10.1016/B978-0-323-90040-9.00028-X.

[27] Y.-F. Huang, et al., Microwave pyrolysis of rice straw to produce biochar as an adsorbent for CO2 capture, Energy 84 (2015) 75–82, https://doi.org/10.1016/j.energy.2015.02.026.

[28] Y.-F. Huang, P.-T. Chiueh, S.-L. Lo, Carbon capture of biochar produced by microwave co-pyrolysis: adsorption capacity, kinetics, and benefits, Environ. Sci. Pollut. Res. 30 (9) (2022) 22211–22221, https://doi.org/10.1007/s11356-022-23734-x.

[29] N.P.F. Gonçalves, S.M. Olhero, J.A. Labrincha, R.M. Novais, 3D-printed red mud/metakaolin-based geopolymers as water pollutant sorbents of methylene blue, J. Clean. Prod. 383 (2023) 135315, https://doi.org/10.1016/j.jclepro.2022.135315.

[30] M.A.O. Lourenco, et al., Biochar/zinc oxide composites as effective catalysts for electrochemical CO2 reduction, ACS Sustain Chem. Eng. 9 (15) (2021) 5445–5453, https://doi.org/10.1021/acssuschemeng.1c00837.

[31] A.L. Myers, Equation of state for adsorption of gases and their mixtures in porous materials, Adsorption 9 (1) (2003) 9–16, https://doi.org/10.1023/A:1023807128914.

[32] A. Nuhnen, C. Janiak, A practical guide to calculate the isosteric heat/enthalpy of adsorption: Via adsorption isotherms in metal-organic frameworks, MOFs, Aug. 14, in: Dalton Transactions, vol. 49, Royal Society of Chemistry, 2020, pp. 10295–10307, https://doi.org/10.1039/d0dt01784a.

[33] H.M.C. Fagnani, C.T.P. da Silva, M.M. Pereira, A.W. Rinaldi, P.A. Arroyo, M.A.S. D. de Barros, CO2 adsorption in hydrochar produced from waste biomass, SN Appl. Sci. 1 (9) (2019) 1031, https://doi.org/10.1007/s42452-019-1055-6.

[34] W. Liang, Z. Liu, J. Peng, X. Zhou, X. Wang, Z. Li, Enhanced CO $_2$ adsorption and CO $_2$ /N $_2$ /CH $_4$ selectivity of novel carbon composites CPDA@A-Cs, Energy Fuels 33 (1) (2019) 493–502, https://doi.org/10.1021/acs.energyfuels.8b03637.

[35] Y. Qiao, S. Zhang, C. Quan, N. Gao, C. Johnston, C. Wu, One-pot synthesis of digestate-derived biochar for carbon dioxide capture, Fuel 279 (2020) 118525, https://doi.org/10.1016/j.fuel.2020.118525.

[36] A.M. Parvez, T. Wu, M.T. Afzal, S. Mareta, T. He, M. Zhai, Conventional and microwave-assisted pyrolysis of gumwood: a comparison study using thermodynamic evaluation and hydrogen production, Fuel Process. Technol. 184 (2019) 1–11, https://doi.org/10.1016/j.fuproc.2018.11.007.

[37] K. Ibraeva, A. Astafev, I. Dimitryuk, R. Tabakaev, I. Kalinich, I. Shanenkov, Comparative analysis of conventional and microwave pyrolysis of raw materials with different degree of metamorphism, Energy Convers. Manag 301 (2024) 118067, https://doi.org/10.1016/j.enconman.2024.118067.

[38] S. Liu, et al., Effects of biochar pyrolysis temperature on thermal properties of polyethylene glycol/biochar composites as shape-stable biocomposite phase change materials, RSC Adv. 12 (16) (2022) 9587–9598, https://doi.org/10.1039/D1RA09167K.

[39] H. Radnia, A.A. Ghoreyshi, H. Younesi, G.D. Najafpour, "Adsorption of Fe(II) ions from aqueous phase by chitosan adsorbent: equilibrium, kinetic, and thermodynamic studies,", Desalin. Water Treat. 50 (1–3) (2012) 348–359, https://doi.org/10.1080/19443994.2012.720112.

[40] H. Rasti, K. Parivar, J. Baharara, M. Iranshahi, F. Namvar, Chitin from the mollusc chiton: extraction, characterization and chitosan preparation. Iran. J. Pharm. Res 16 (1) (2017) 366–379.

[41] M. El-Shahate Ismaiel Saraya, H. Hassan Abdel Latif Rokbaa, Preparation of vaterite calcium carbonate in the form of spherical nano-size particles with the aid of polycarboxylate superplasticizer as a capping agent, Am. J. Nanomater. 4 (2) (2016) 44–51, https://doi.org/10.12691/ajn-4-2-3.

[42] J.J. Manyà, B. González, M. Azuara, G. Arner, Ultra-microporous adsorbents prepared from vine shoots-derived biochar with high CO2 uptake and CO2/N2 selectivity, Chem. Eng. J. 345 (2018) 631–639, https://doi.org/10.1016/j.cej.2018.01.092.

[43] P. Maziarka, C. Wurzer, P.J. Arauzo, A. Dieguez-Alonso, O. Mašek, F. Ronsse, Do you BET on routine? The reliability of N2 physisorption for the quantitative assessment of biochar's surface area, Chem. Eng. J. 418 (2021), https://doi.org/10.1016/j.cej.2021.129234.

[44] S. Dantas, K.C. Struckhoff, M. Thommes, A.V. Neimark, Pore size characterization of micro-mesoporous carbons using CO2 adsorption, Carbon 173 (2021) 842–848, https://doi.org/10.1016/j.carbon.2020.11.059.

[45] P.I. Ravikovitch, A. Vishnyakov, R. Russo, A.V. Neimark, Unified approach to pore size characterization of microporous carbonaceous materials from N2, Ar, and CO2 adsorption isotherms, Langmuir 16 (5) (2000) 2311–2320, https://doi.org/10.1021/la991011c.

[46] Y. Qiao, C. Wu, Nitrogen enriched biochar used as CO2 adsorbents: a brief review, Carbon Capture Sci. Technol. 2 (2022) 100018, https://doi.org/10.1016/j.ccst.2021.100018.

[47] T. Watabe, K. Yogo, Isotherms and isosteric heats of adsorption for CO2 in amine-functionalized mesoporous silicas, Sep Purif. Technol. 120 (2013) 20–23, https://doi.org/10.1016/j.seppur.2013.09.011.

[48] V. Gargiulo, A. Gomis-Berenguer, P. Giudicianni, C.O. Ania, R. Ragucci, M. Alfè, Assessing the potential of biochars prepared by steam-assisted slow pyrolysis for CO $_2$ adsorption and separation, Energy Fuels 32 (10) (2018) 10218–10227, https://doi.org/10.1021/acs.energyfuels.8b01058.

[49] C. Dhoke, A. Zaabout, S. Cloete, S. Amini, Review on reactor configurations for adsorption-based CO $_2$ capture, Ind. Eng. Chem. Res 60 (10) (2021) 3779–3798, https://doi.org/10.1021/acs.iecr.0c04547.

[50] S.J.A. DeWitt, A. Sinha, J. Kalyanaraman, F. Zhang, M.J. Realff, R.P. Lively, Critical comparison of structured contactors for adsorption-based gas separations, Annu Rev. Chem. Biomol. Eng. 9 (1) (2018) 129–152, https://doi.org/10.1146/annurev-chembioeng-060817-084120.

[51] N.P.F. Gonçalves, E.F. da Silva, L.A.C. Tarelho, J.A. Labrincha, R.M. Novais, Simultaneous removal of multiple metal(loid)s and neutralization of acid mine drainage using 3D-printed bauxite-containing geopolymers, J. Hazard Mater. 462 (2024) 132718, https://doi.org/10.1016/j.jhazmat.2023.132718.

[52] G. Franchin, et al., Removal of ammonium from wastewater with geopolymer sorbents fabricated via additive manufacturing, Mater. Des. 195 (2020), https://doi.org/10.1016/j.matdes.2020.109006.

[53] H. Chen, S. Dong, Y. Zhang, P. He, Robust structure regulation of geopolymer as novel efficient amine support to prepare high-efficiency CO2 capture solid sorbent, Chem. Eng. J. 427 (2022) 131577, https://doi.org/10.1016/j.cej.2021.131577.

[54] A.L. Freire, H.J. José, R. de F.P.M. Moreira, Potential applications for geopolymers in carbon capture and storage, Int. J. Greenh. Gas. Control 118 (2022) 103687, https://doi.org/10.1016/j.ijggc.2022.103687.

[55] J. Xu, et al., Research and application progress of geopolymers in adsorption: a review, Nanomaterials *12* (17) (2022) *3002*, https://doi.org/10.3390/NANO12173002.

[56] M. El Alouani, et al., Application of geopolymers for treatment of water contaminated with organic and inorganic pollutants: state-of-the-art review, J. Environ. Chem. Eng. 9 (Apr. 01, 2021), https://doi.org/10.1016/j.jece.2021.105095.

[57] R.M. Novais, Robert C. Pullar, J.A. Labrincha, Geopolymer foams: an overview of recent advancements, Prog. Mater. Sci. 109 (2020) 100621, https://doi.org/10.1016/j.pmatsci.2019.100621.